

Chapter 8

Steel–Concrete–Steel Sandwich Panel Under Simulated Blast Loading



8.1 Introduction

Steel–concrete–steel (SCS) sandwich structure, which consists of a concrete core connected to two external steel faceplates using mechanic shear connectors, exhibited superior ductility and strength as compared to conventional reinforced concrete structures. The potential applications of SCS structures in resisting static, impact and blast loads have been demonstrated in previous studies (Liew and Sohel 2009; Sohel and Liew 2011; Liew et al. 2009; Remennikov and Kong 2012; Anandavalli et al. 2012; Wang et al. 2015b; Crawford and Lan 2006; Liew and Wang 2011; Lan et al. 2005). In the past, the SCS sandwich structure was applied to sustain static and impact loads, while the application has been extended to protective layer against blast loading owing to its high energy absorption capacity and scabbing protection (Anandavalli et al. 2012; Wang et al. 2015b; Crawford and Lan 2006; Liew and Wang 2011; Lan et al. 2005). Most reported works on SCS sandwich structures involved the use of mechanical shear connectors, whereas there was a lack of study on the performance of non-composite SCS sandwich panel under blast loading (Liew and Wang 2011), and its energy absorption performance was also not fully understood. Hence, the laboratory tests (by using a drop-weight impact test system and inflated airbag) were carried out to investigate the response of the non-composite SCS sandwich panel under simulated blast loading. Moreover, its energy absorption performance was further revealed by conducting numerical simulations using LS-DYNA which has been widely employed for simulating blast and impact responses of civil infrastructures, including concrete (Tabatabaei et al. 2013; Wu and Chew 2014; Lin et al. 2014; Mao et al. 2014; Chen et al. 2015; Jiang et al. 2012), steel (Zhai et al. 2013; Zhai and Wang 2013) and sandwich structures (Jing et al. 2013; Hou et al. 2013; Kilicaslan et al. 2013).

A blast is characterized by a rapid expansion of gas, generating a pressure wave propagating from the source of the explosion (Smith et al. 2009). The effect of a blast is in the form of a shock wave composed of a high-intensity shock front which expands outward from the surface of the explosive into the surrounding air. As the

wave expands, it decays in strength, lengthens in duration, and decreases in velocity (UFC 2008). The shape of the blast wave depends on the nature of the energy release. When the explosive is located on or near to the ground, the blast is considered to be a surface burst. The incident blast wave is reflected and amplified by the ground, and the reflected wave then merges with the incident wave to form a hemispherical blast wave. When the explosive is far from any reflecting surface, the blast is considered to be an air burst and is a spherical blast wave (Smith and Hetherington 1994).

The typical pressure–time profile for the blast wave in free air is shown in Fig. 8.1, which includes positive and negative phase. In the positive phase, the incident pressure (P_s) decays to the ambient pressure (P_o) within the time duration t_d (i.e., positive phase duration). For the following negative phase, the peak negative pressure is typically small as compared to the peak pressure in positive phase. Hence, the negative phase is usually ignored in the blast resistant design (UFC 2008; ASCE 2010, 2011). The positive phase of surface blast can be described by the modified Friedlander Equation (Baker 1973) as:

$$P(t) = P_r \left(1 - \frac{t}{t_d} \right) \exp \left(-\frac{\bar{\theta} t}{t_d} \right) \quad (8.1)$$

where $\bar{\theta}$ is the coefficient that describes the rate of decay of the pressure–time curve. The parameters P_r , t_d and $\bar{\theta}$ can be obtained using blast loading predictive tool CONWEP (Hyde 1991) by given TNT charge and standoff distance. Herein the reflected pressure P_r is used, as the blast wave is reflected and magnified with higher reflected pressure when it impinges onto the face of a target. In the blast resistant design, the pressure–time profile in positive phase can be further simplified as a bi-linear or triangular shape (UFC 2008; ASCE 2011).

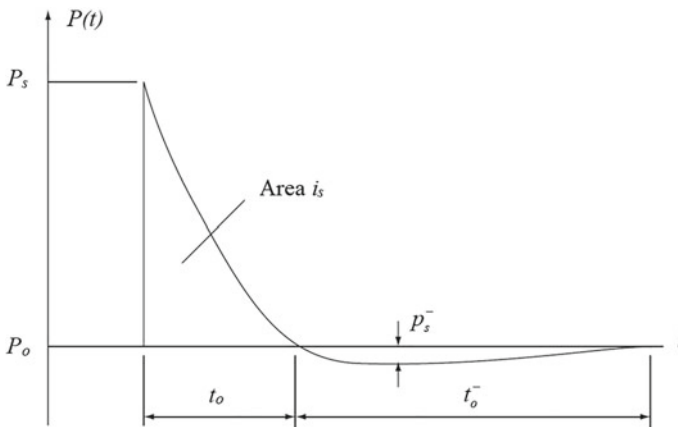


Fig. 8.1 Typical pressure–time profile for blast wave in free air (Smith and Hetherington 1994)

Field blast test is a method to directly apply blast loading on structures (Clubley 2014; Foglar and Kovar 2013; Arora et al. 2011). This method is able to replicate the actual condition of the detonation of high explosives and can be used to test several specimens simultaneously. However, field blast test is generally expensive and requires remote testing site. Besides, the test data may be easy to lose due to the damage of transducers, cables or data acquisition equipment. Therefore, other methods such as shock tube and non-explosive test method have been devised to simulate the high pressure and short duration of a blast loading. In the shock tube test method, which is generally less expensive than the field blast test, the generated impulse loading can be well controlled. However, the specimen size is limited by the size of the shock tube, and the load duration is relatively longer compared with the field blast test (Lacroix et al. 2014; Schleyer et al. 2007). In the absence of field blast test and shock tube facilities, Mostaghel (2003) developed a simple non-explosive test method for generating impulsive loading by using a membrane formed inflated airtight chamber mounted to a frame system. A plate was dropped onto the membrane from various heights to achieve the required impulse magnitude and duration. Even though the load duration is longer than that generated by the field blast detonation, this method is simple and can be easily conducted in the laboratory, and therefore was adopted by some researchers to generate blast-type pressure loading (Chen and Hao 2014; Remennikov et al. 2009). Remennikov et al. (2009) adapted this method with an inflated airbag acting as the airtight chamber to test columns under impulse loading. The similar method was also employed by Chen and Hao (2014) to investigate the response of multi-arch double-layered panels under impulse loading. As the use of airbag to generate pressure loading in the laboratory appeared to be an easy and economical way, a similar concept was employed in this study by using high pressure airbag to test the SCS sandwich panels under impact-induced impulsive loading. The airbag was charged with initial pressure of 100 kPa before impact to reduce the loading duration to 0.042–0.049 s, which was shorter than those reported by Chen and Hao (2014) and Remennikov et al. (2009).

8.2 Experimental Study

8.2.1 Design of Specimens

Two SCS sandwich panels with different concrete core depths of 50 (SCS50) and 75 mm (SCS75) were fabricated from mild steel plates that were fillet welded together to form the outer skin, as shown in Fig. 8.2. A 32 mm (1¼ inch) inlet pipe with stopper ball valve and a 32 mm (1¼ inch) outlet pipe with threaded cap were provided at the side and end plates of the panels for pumping of cement grout into the core during casting. The schematic drawing of the panel is shown in Fig. 8.3, and the details are summarized in Table 8.1.

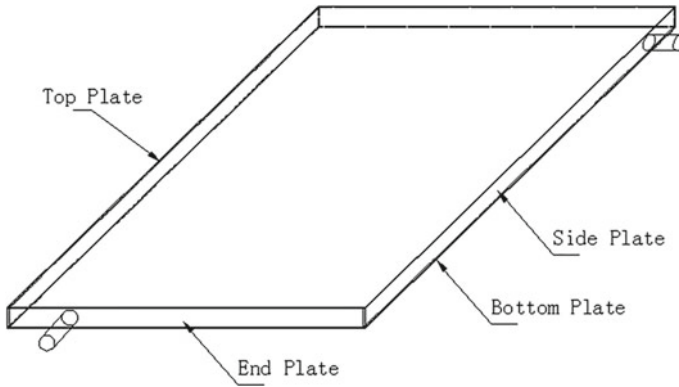


Fig. 8.2 Notation for SCS sandwich panel, reprinted from Wang et al. (2015a), copyright 2022, with permission from Elsevier

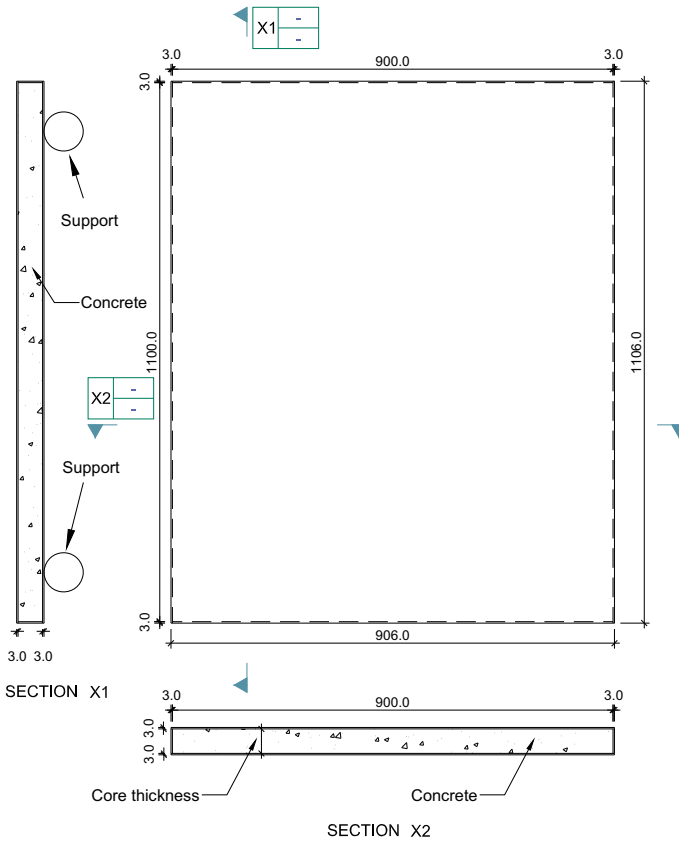


Fig. 8.3 Schematic drawing of SCS sandwich panel, reprinted from Wang et al. (2015a), copyright 2022, with permission from Elsevier

Table 8.1 Details of SCS sandwich panels

Label	Length × width (mm)	$t_s-t_c-t_s$ (mm)	Material strength	
			Mild steel	Grout
SCS50	1100 × 900	3-50-3	f_y (MPa)	f_u (MPa)
SCS75		3-75-3	309	50

Note t_s, t_c —face plate thickness and core depth; f_y, f_u —yield stress and ultimate stress of steel

8.2.2 Test Setup and Instrumentation

The instrumented drop-weight impact test machine that was used to apply the impact-induced impulsive loading in the laboratory is shown in Fig. 8.4. A hydraulic controlled mechanical hoisting system is utilized to raise the projectile up to 4 m height. Once the winch brake is released, the projectile, which has an adjustable weight of 500–1200 kg, will slide down freely along the vertical guide rails. The SCS panel was placed below the projectile and simply supported on two 80-mm-diameter bars support with clear span of 900 mm, as shown in Fig. 8.5. The inflated height of the airbag between the impact plate (with size of 1000 × 1000 × 30 mm) and SCS panel was kept at 160 mm by using two wood beams that were inserted between the frame and impact plate. The airbag was charged with initial pressure of 100 kPa before impact. Even though the change in contact area between the airbag and SCS panel during impact test was expected to be less significant if higher initial pressure

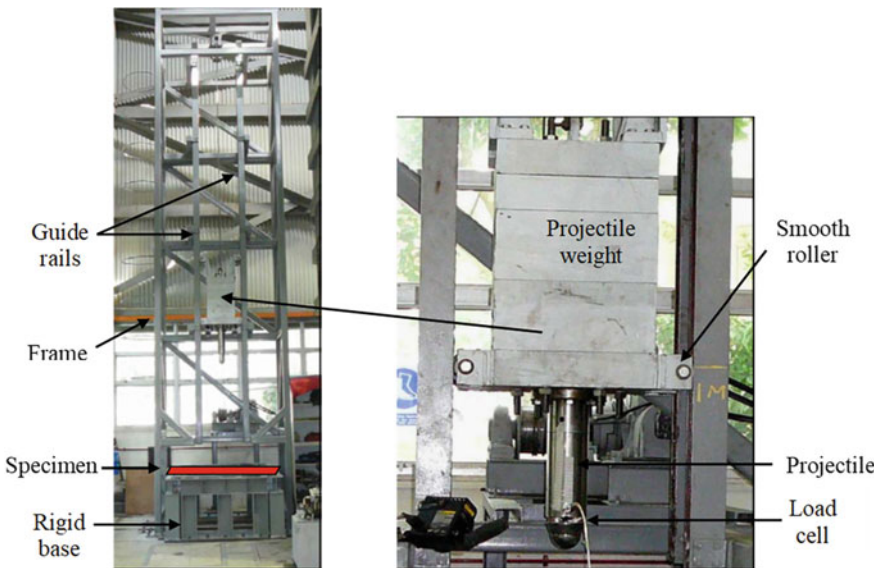


Fig. 8.4 Drop-weight impact test machine, reprinted from Wang et al. (2015a), copyright 2022, with permission from Elsevier

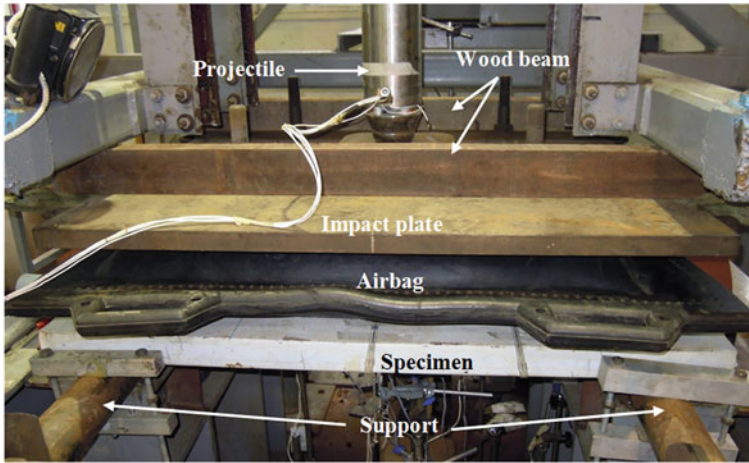


Fig. 8.5 Test setup, reprinted from Wang et al. (2015a), copyright 2022, with permission from Elsevier

of airbag was applied, the current initial pressure (100 kPa) was selected such that the midpoint displacement of specimen was minimal (less than 2 mm) and within the elastic range. Wet paint was applied to the bottom surface of the inflated airbag which was not in contact with the SCS panel before test. As the wet paint would leave a marking on the SCS panel after impact test, the maximum contact area during impact could be determined. The inflated height of 160 mm was selected based on trial tests and kept as small as possible, since an inflated airbag with lower compressibility, which can be defined as the ratio of compression distance of airbag, ΔH , to change of air pressure, ΔP , will generate impulsive loading with shorter duration.

A digital circuit in combination with laser emitters and photodiodes was used to measure impact velocity of the projectile just before the impact and also to trigger the data acquisition system of the 16-channel Oscilloscope 1 with sampling rate of 1 MHz, as shown in Fig. 8.6. The Dytran high frequency 2300 V Low Impedance Voltage Mode (LIVM) pressure sensor was connected to the inlet pipe of the airbag to capture the air pressure, and three quartz force rings on the same plane with total capacity of 1050 kN were attached to the projectile to record the impact force. The displacement and strain responses of the specimen were respectively measured by using potentiometers and strain gauges at the positions shown in Fig. 8.7. The signals from the photodiodes, pressure sensor, quartz force rings and potentiometers were captured using Oscilloscope 1 while the strain gauge readings were recorded by the 16-channel Oscilloscope 2 with the sampling rate of 1 MHz. Oscilloscope 2 was triggered by the strain gauge S0 at the mid-span.

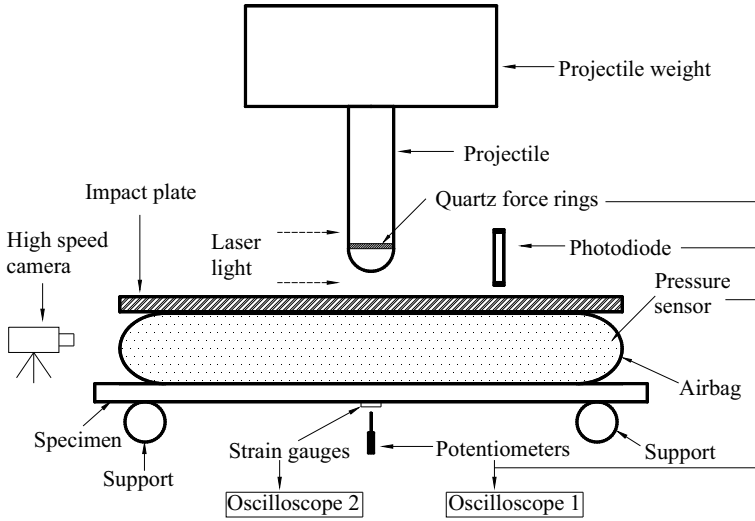


Fig. 8.6 Overview of data acquisition system, reprinted from Wang et al. (2015a), copyright 2022, with permission from Elsevier

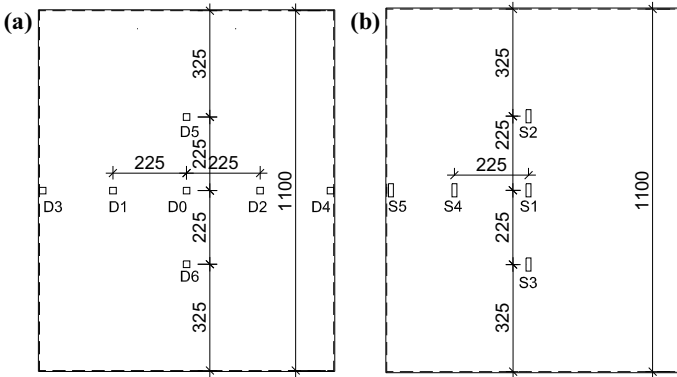


Fig. 8.7 Instrumentation layout (bottom view): **a** potentiometers and **b** strain gauges, reprinted from Wang et al. (2015a), copyright 2022, with permission from Elsevier

8.2.3 Test Results and Discussions

The SCS50 and SCS75 sandwich panels were subjected to impact by an 800 kg projectile that was dropped from the height of 3.7 m. The impact force, air pressure, deformation and strain responses were measured in the test and are discussed as follows.

8.2.3.1 Impact Force and Air Pressure

The recorded impact force–time histories between the projectile and impact plate are plotted in Fig. 8.8. Multiple contacts between the two can be seen from the plots, since the heavier projectile continued to move downwards and hit the impact plate again multiple times after the first contact. The air pressure–time histories, which represent the impulsive loading acting on the SCS panel, are plotted in Fig. 8.9. The measured loading durations for the SCS50 and SCS75 panels are 0.049 and 0.042 s, respectively, which are shorter than those reported by Chen and Hao (2014) and Remennikov et al. (2009). The shorter duration can be attributed to the higher initial pressure and drop weight used in the current test. The recorded impact velocity (V), maximum impact force (F_{max}), impact impulse (I) and maximum air pressure (P) are summarized in Table 8.2. The impact impulse was obtained by integrating the impact force–time curve shown in Fig. 8.8. From Table 8.2, it appears that the SCS75 panel with higher resistance and mass absorbed higher impact impulse under the same impact condition.

Fig. 8.8 Impact force–time history of SCS sandwich panels, reprinted from Wang et al. (2015a), copyright 2022, with permission from Elsevier

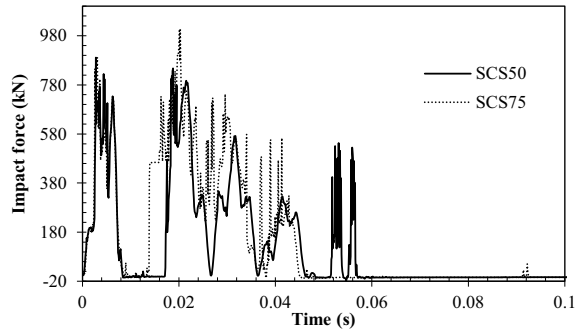


Fig. 8.9 Pressure–time history of SCS sandwich panels, reprinted from Wang et al. (2015a), copyright 2022, with permission from Elsevier

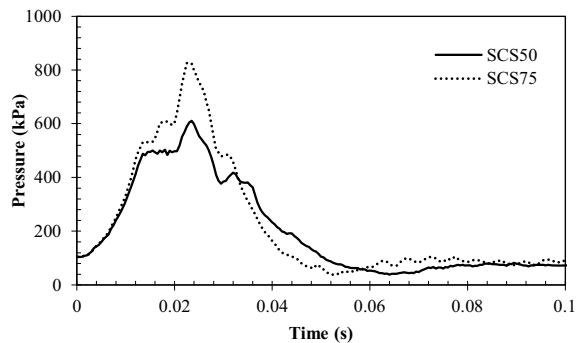


Table 8.2 Summary of test results

Specimen	V (mm/s)	F_{max} (kN)	I (Ns)	P (kPa)	D_{max} (mm)	D_{perm} (mm)
SCS50	8147	895	12,837	617	34.7	20.4
SCS75	8070	1012	15,703	829	9.8	3.9

Note V —Impact velocity; F_{max} —Maximum impact force; I —Impact impulse; P —Maximum pressure; D_{max} , D_{perm} —maximum and permanent displacement

8.2.3.2 Deformation Response

The deformation mode of the SCS50 panel under the impact-induced impulsive loading was a combination of flexure and shear, as shown in Fig. 8.10. Bulging near the support line was visible, which could be due to the expansion of grout after cracking under shear deformation. Comparison of the permanent deformation of SCS50 and SCS75 sandwich panels in Fig. 8.11 shows that the deformation was considerably reduced by increasing the concrete core depth owing to the increase in resistance and mass. However, the possibility of brittle shear failure may be increased

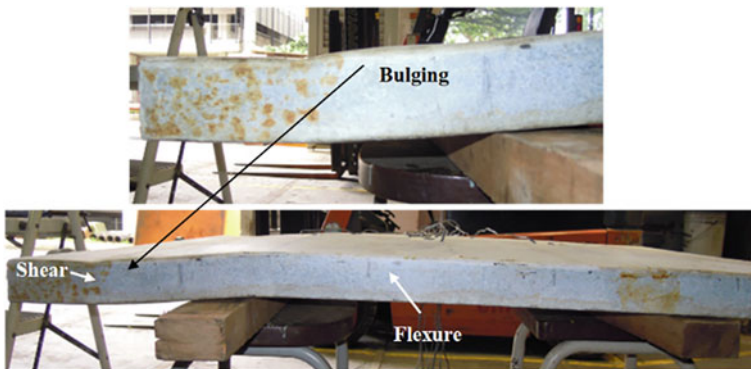


Fig. 8.10 Deformed shape of SCS50 sandwich panel after test, reprinted from Wang et al. (2015a), copyright 2022, with permission from Elsevier



Fig. 8.11 Comparison of permanent deformation of SCS50 and SCS75 sandwich panels after test, reprinted from Wang et al. (2015a), copyright 2022, with permission from Elsevier

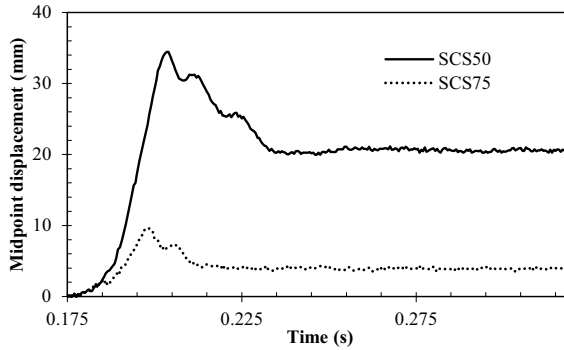


Fig. 8.12 Displacement–time histories of SCS50 and SCS75 sandwich panels, reprinted from Wang et al. (2015a), copyright 2022, with permission from Elsevier

with increasing core depth. Therefore, it is important to ensure that the SCS sandwich panel with thicker concrete core has sufficient shear resistance to avoid shear failure.

Figure 8.12 compares the midpoint displacement–time histories of the SCS50 and SCS75 sandwich panels, and the maximum displacement of the SCS50 sandwich panel is about 3.5 times higher than that of SCS75 sandwich panel. The maximum displacements occurred at their first peaks in the curves, which are consistent with the recorded pressure–time histories. As shown in Table 8.2, the permanent midpoint displacement of the SCS75 sandwich panel was significantly less than that of SCS50 sandwich panel.

8.2.3.3 Strain Response

Figure 8.13 presents the longitudinal strain distribution (S1, S4 and S5) across the width of the SCS50 panel. The three strain readings were initially similar at the beginning of loading. As the load increases, the strain reading of S5 near the side plate continued to increase while there were no significant changes to the S1 and S4 readings after a sudden drop in strain at 0.187 s. This observed difference in the strain development and the sudden drop of strain value were likely due to the weakened composite action of the SCS panel without shear connectors after debonding of the grout core from the bottom plate. Another sudden drop was observed at 0.190 s, which indicates the progressive debonding between the grout and bottom plate with continuous impact. Similarly for the SCS75 panel, the strain reading of S5 near side plate continued to rise at higher rate than those of S1 and S4 after the sudden drop caused by debonding, as shown in Fig. 8.14. In the span direction (S1, S2 and S3), the mid-span strain reading S1 was higher than the quarter-span strains S2 and S3 for both the SCS50 and SCS75 panels before the debonding. However, higher strain readings were observed at the quarter-spans after debonding. This indicates that the debonding between grout core and bottom plate affected the strain development at the bottom plate of the SCS panels.

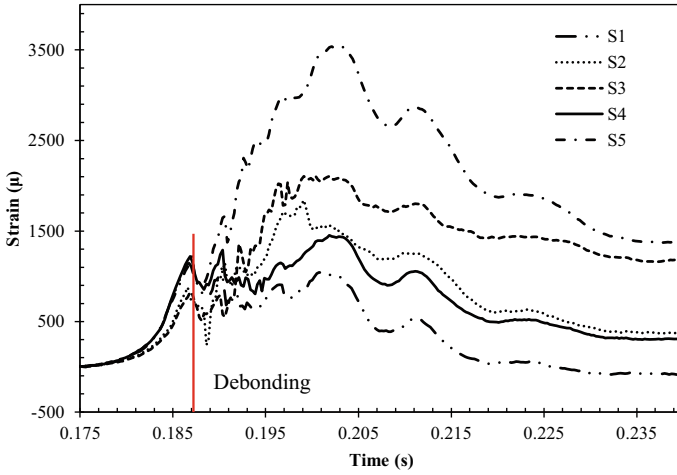


Fig. 8.13 Longitudinal strain–time history of SCS50 sandwich panel, reprinted from Wang et al. (2015a), copyright 2022, with permission from Elsevier

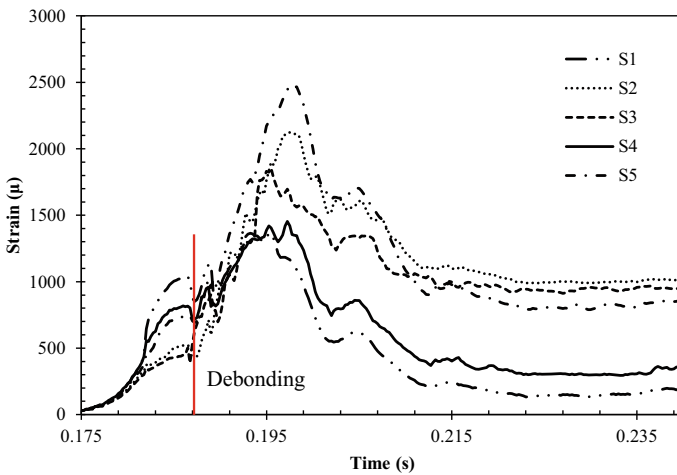


Fig. 8.14 Longitudinal strain–time history of SCS75 sandwich panel, reprinted from Wang et al. (2015a), copyright 2022, with permission from Elsevier

8.3 Numerical Study

Following the laboratory test, the explicit code in LS-DYNA (Hallquist 2012) was employed to simulate the SCS sandwich panels under both impulsive loading and actual blast loading.

8.3.1 Material Models

8.3.1.1 Grout Material

Concrete and other cement-based material (like grout) are heterogeneous materials that exhibit nonlinear inelastic behavior under multi-axial stress states. To accurately predict the material responses and failure modes under various loading scenarios, the key material characteristics have to be captured in the constitutive model, including the influence of confinement on strength and energy absorption capacity, compression hardening and softening behaviors, volumetric expansion upon cracking, tensile fracture and softening, biaxial response and strain rate effects under dynamic load (Crawford et al. 2012). In the current study, the Karagozian & Case concrete model (MAT_72R3) in LS-DYNA, which was developed by Malvar et al. (1997), was adopted to model the grout.

The deviatoric strength of MAT_72R3 is defined by three independent failure surfaces, including the initial yield surface, maximum failure surface and residual surface, which are written as follow (Magallanes et al. 2010):

$$\nabla\sigma_i(p) = a_{0i} + \frac{p}{a_{1i} + a_{2i}p} \quad (8.2)$$

where p is hydrostatic pressure, and a_{0i} , a_{1i} and a_{2i} are parameters that define the failure surfaces.

For hardening, the current failure surface is linearly interpolated between the yield and maximum surfaces based on the value of damage parameter η , as given in Eq. (8.3). A similar interpolation is performed between the maximum and residual surfaces for softening in Eq. (8.4).

$$\Delta\sigma = \eta(\Delta\sigma_m - \Delta\sigma_y) + \Delta\sigma_y \quad (8.3)$$

$$\Delta\sigma = \eta(\Delta\sigma_m - \Delta\sigma_r) + \Delta\sigma_r \quad (8.4)$$

In above equations, $\Delta\sigma_y$, $\Delta\sigma_m$ and $\Delta\sigma_r$ are the yield, maximum and residual surfaces, and η varies between 0 and 1 depending on the accumulated effective plastic strain parameter λ , which is defined as

$$\lambda = \int_0^{\varepsilon_p} \frac{d\varepsilon_p}{r_f(1 + p/r_f f_t)^{b_1}} \quad \text{for } p \geq 0 \quad (8.5)$$

$$\lambda = \int_0^{\varepsilon_p} \frac{d\varepsilon_p}{r_f(1 + p/r_f f_t)^{b_2}} \quad \text{for } p < 0 \quad (8.6)$$

where r_f is the strain rate enhancement factor, b_1 and b_2 are the damage scaling exponents, and $d\varepsilon_p = \sqrt{(2/3)\varepsilon_{ij}^p\varepsilon_{ij}^p}$ is the effective plastic strain increment. The damage scaling exponents b_1 and b_2 govern the softening of unconfined uniaxial stress–strain curve in compression and tension, respectively (Malvar et al. 1997). To ensure constant fracture energy dissipation, b_2 is determined by iterative calculation until the area under the stress–strain curve for a uniaxial unconfined tensile test coincides with G_f/h , where G_f and h are the fracture energy and element size, respectively. Similarly, b_1 is determined using uniaxial unconfined compressive test. In this study, the fracture energy from uniaxial unconfined compressive test on the grout was used to determine b_1 . The fracture energy of grout in tension-softening given by Ishiguro (2007) in Eq. (8.7) was used to determine b_2 .

$$G_f = 0.0251 f_c^{0.105} \tag{8.7}$$

where f_c is the compressive strength of grout in MPa.

The volumetric response of the grout material is defined using the tabulated Equation of State (EOS), numbered as EOS_8 in LS-DYNA. The EOS relates the hydrostatic pressure, p , the relative volume, V , and the internal energy, e_i . In the loading (compression) phase, the pressure is defined as

$$p = C(\varepsilon_v) + \gamma T(\varepsilon_v)e_i \tag{8.8}$$

where ε_v is the natural logarithm of the relative volume, C and T are coefficients given as function of ε_v , and e_i is the internal energy. Unloading occurs at the slope corresponding to the bulk modulus at the peak (most compressive) volumetric strain. Reloading follows the unloading path to the point where unloading begins and continues on the loading path (Hallquist 2006). In this study, the thermal state of grout $\gamma T(\varepsilon_v)e_i$ in Eq. (8.8) was not considered, and the values of C and ε_v can be generated by using the automated generation option in MAT_72R3, which is based on uniaxial strain test on normal concrete (Malvar et al. 1997). The bulk modulus of the grout (13.83 GPa) was determined from uniaxial unconfined compressive test and was applied in the parameters in the EOS_8. Other material properties of the grout are also tabulated in Table 8.3.

The strain rate effect was captured in MAT_72R3 by modifying the failure surface and damage function λ through the modified damage function in Eqs. (8.5) and (8.6).

Table 8.3 Material properties of grout and mild steel

Material	ρ (kg/m ³)	f_c/f_y (MPa)	E (GPa)	μ
Grout	2150	50.3	24.9	0.2
Steel	7850	309.2	205.2	0.28

Note ρ —Density; f_c/f_y —Compressive stress of grout/yield stress of mild steel; E —Young’s modulus; μ —Poisson’s ratio

A radial rate enhancement on the concrete failure surface was implemented, and the enhanced strength $\Delta\sigma_e$ corresponding to pressure p is determined as follow (Malvar et al. 1997):

$$\Delta\sigma_e = \gamma_f \Delta\sigma(p/\gamma_f) \quad (8.9)$$

where γ_f is the strain rate enhancement factor or Dynamic Increase Factor (DIF). The DIF–strain rate in Eq. (8.10) (Grote et al. 2001) was adopted in the current study for the grout in compression

$$DIF = \begin{cases} 0.0235 \log \dot{\epsilon} + 1.07 & (\dot{\epsilon} < 250) \\ 0.882(\log \dot{\epsilon})^3 - 4.48(\log \dot{\epsilon})^2 + 7.22 \log \dot{\epsilon} - 2.64 & (\dot{\epsilon} \geq 250) \end{cases} \quad (8.10)$$

For tension, the DIF–strain rate in Eq. (8.11) was obtained for the grout by fitting the experimental data from Ross et al. (1989).

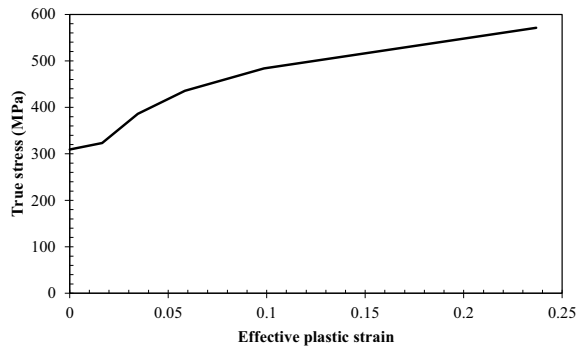
$$DIF = \exp\left\{0.0513[\log(\dot{\epsilon}/\dot{\epsilon}_s)]^{1.35}\right\} \quad (8.11)$$

where $\dot{\epsilon}_s = 1\text{E-}7$.

8.3.1.2 Steel Material

The Piecewise Linear Plasticity material model was adopted to simulate the mild steel material. The material properties given in Table 8.3 were determined from the tensile coupon tests, and the input true stress–effective plastic strain curve is given in Fig. 8.15. The strain rate effect of mild steel was considered by using the Cowper–Symonds model, as defined in Eq. (1.8). Jones (1988) obtained the values of $C = 40.4 \text{ s}^{-1}$ and $p = 5$ for the mild steel by fitting the experimental data assembled by

Fig. 8.15 The input true stress–effective plastic strain curve of mild steel, reprinted from Wang et al. (2015a), copyright 2022, with permission from Elsevier



Symonds (1967). There is however, a considerable scatter to the data, which may be related to the different mild steels used in the experiments. As such, using these values may overestimate the strain rate effects of some kinds of mild steels. More recently, the values of $C = 802 \text{ s}^{-1}$ and $p = 3.585$ were determined by Abramowicz and Jones (1986) from dynamic uniaxial tensile tests. These values were employed for the mild steel in the current study to reduce the possibility of overestimating the strain rate effects owing to the lack of dynamic test data for the current mild steel.

8.3.2 Model Description

Since the applied impulsive pressure loading on the SCS panel can be represented by the measured air pressure–time history, only the parts shown in Fig. 8.16 were included in the FE model. Owing to symmetry, a quarter FE model of the SCS sandwich panel with round bars as support was modeled, as shown in Fig. 8.17. The nodes along the bottom of the round bars support were restricted from translation and rotation in the model to simulate the fixed round bar support. Since the airbag was flexible and has negligible contribution to the resistance of the SCS sandwich panel, it was not explicitly modeled. However, the mass of the bottom airbag skin that was in contact with the SCS panel was included in the FE model, because it moved together with the SCS panel and would increase the total mass, and thus affecting the

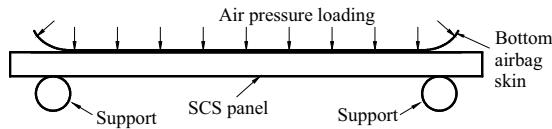


Fig. 8.16 Simplification of FE simulation, reprinted from Wang et al. (2015a), copyright 2022, with permission from Elsevier

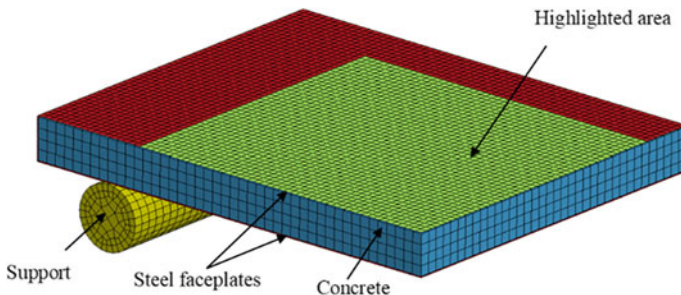


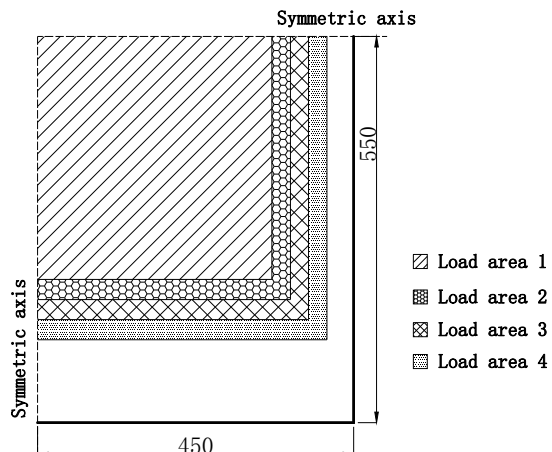
Fig. 8.17 FE model of SCS sandwich panel, reprinted from Wang et al. (2015a), copyright 2022, with permission from Elsevier

structural response under impulsive loading. This was done by increasing the density of the highlighted elements of the top plate in Fig. 8.17 with additional mass.

Since the contact area between the airbag and specimen varied continuously during the test and only the contact areas corresponding to initial pressure and maximum pressure were recorded, a linear relationship between the contact area and pressure was assumed to obtain the contact area–time history during the test. The applied force–time history was then determined by multiplying the pressure with the contact area. Four contact areas were selected in the FE model to represent the variation of contact area, as illustrated in Fig. 8.18 for the SCS50 panel. The applied pressure–time histories on each load area were increased from zero. The total applied force–time history in the FE model was checked against the recorded applied force–time history, and they were kept to be identical. Dynamic relaxation approach was utilized to treat the initial static pressure that applied on the SCS sandwich panels before impact test.

The steel plates of the SCS sandwich panel were meshed using S/R Hughes-Liu shell element, and eight-node brick element with reduced integration was employed for the grout core and bar support (Hallquist 2012). The penalty-based contact approach, which is suitable for modeling contact between bodies of similar materials, was adopted for the contact between faceplates and support. The soft constraint-based contact approach, which is suitable for treating contact between bodies of dissimilar materials, was employed for the contact between faceplates and grout core. Since no shear connectors were used in the SCS panel, the bonding strength between the grout core and faceplates was only contributed by the adhesive strength of grout. This weak bonding strength was ignored in the analysis as it has little effect on the displacement response of the SCS panel under impulsive loading owing to the relatively longer loading duration as compared to the natural period of the SCS panel.

Fig. 8.18 Varying load area in the FE model of SCS50 sandwich panel (quarter model), reprinted from Wang et al. (2015a), copyright 2022, with permission from Elsevier



8.3.3 Numerical Results and Discussions

The FE-predicted midpoint displacement–time histories of the SCS50 and SCS75 panels are compared with test results in Fig. 8.19. Reasonably well prediction of the displacement–time history of SCS50 panel can be seen in the comparison. Although the FE model overestimates the maximum displacement of SCS75 panel by 26.7%, the simulated permanent displacement matches closely with test result. The over-predictions by FE analyses may be due to the adopted strain rate parameters for the mild steel and geometric imperfection of the SCS panel. The midpoint displacements of both SCS50 and SCS75 sandwich panels in the tests continuously increase to their maximum values, whereas the displacement–time histories given by FE analyses show some fluctuating before reaching their maximum values. The reason is that the damping, which may eliminate the fluctuating of specimen in the test, is not incorporated into the FE model. This can also explain the higher magnitude of fluctuating of FE-predicted curves as compared to tests after the maximum displacement.

The FE-calculated internal energies of steel and grout materials in the SCS50 panel and their ratios are presented in Fig. 8.20. The internal energy of steel was higher than grout at the beginning, which may be attributed to the sudden applied impulsive loading on the top plate of the SCS panel. Subsequently, both the steel plates and grout core produced comparable internal energies with increasing deformation of the SCS panel. Finally, more internal energy was dissipated by the steel plates, and the

Fig. 8.19 Comparison of FE predicted displacement–time histories with test results: **a** SCS50, **b** SCS75, reprinted from Wang et al. (2015a), copyright 2022, with permission from Elsevier

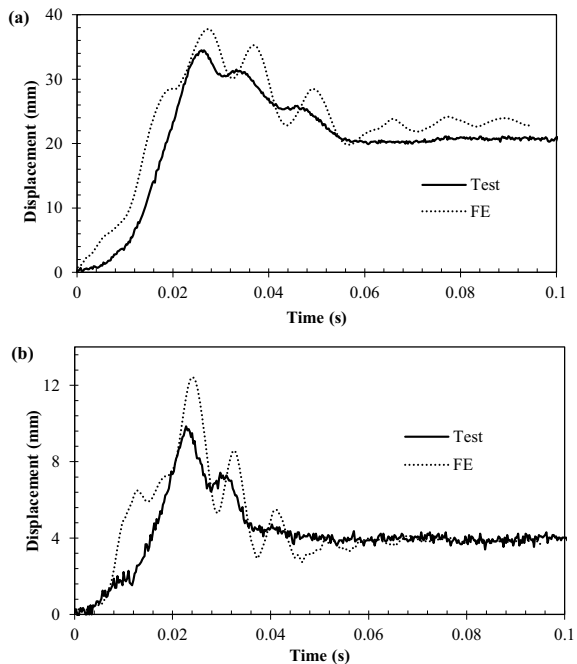
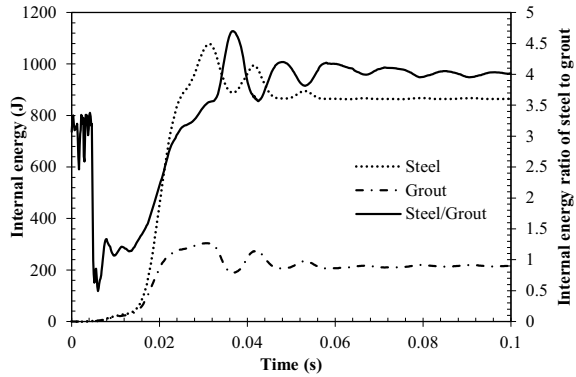


Fig. 8.20 Internal energy of steel and grout material of SCS50 sandwich panel, reprinted from Wang et al. (2015a), copyright 2022, with permission from Elsevier



internal energy ratio of steel to grout was almost constant at 4.0. This was expected as the steel plate has higher strength and ductility as compared to the grout core. Although the energy absorption capacity of the grout is lower than steel plate, it helped to resist the buckling of faceplates and increase the total mass of the SCS panel.

8.3.4 Further Numerical Simulations and Discussions

The measured loading durations in the test ranged from 0.042 to 0.049 s for the two SCS sandwich panels. This loading duration is longer compared with the typical blast loading. For instance, the loading duration of 100-kg TNT charge detonated at 10 m away is 0.0097 s. The experimentally-verified FE models were utilized herein to investigate the performance of the SCS sandwich panel under blast loading. The same quarter FE model presented in Sect. 8.3 were used in the following analysis. The loading was changed to blast pressure loading which was applied on the whole top face of the SCS sandwich panel. The adopted blast pressure–time history has an exponential decay from peak pressure P_r to ambient pressure at time t_d . Negative pressure was omitted as it has little effect on the structural response and is normally neglected in the blast resistant design (UFC 2008; ASCE 2010, 2011). The positive phase can be described by the modified Friedlander equation (Baker 1973) as given in Eq. (8.1). In this analysis, 100-kg TNT charge detonated at 10 m away was adopted, and the peak pressure P_r , load duration t_d and decay coefficient θ were obtained as 845.5 kPa, 9.7 ms and 2.4, respectively, by using CONWEP (Hyde 1991).

In the impact tests, the simply supported boundary condition for SCS sandwich panels were employed, as the axially-restrained boundary conduction is generally difficult to be achieved. However, the axially-restrained boundary condition is preferred in actual applications owing to the enhanced blast resistance of SCS sandwich panels via tensile membrane effect of faceplates. Hence, the FE simulations

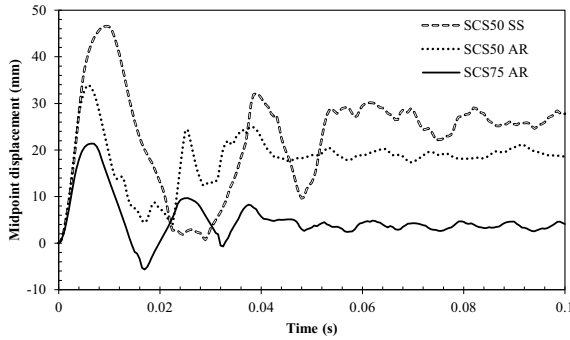


Fig. 8.21 Midpoint displacement–time histories of SCS sandwich panels under blast loading (SS–Simply support; AR–Axially restrained)

were conducted to investigate the response of axially-restrained SCS sandwich panels under blast loading. The midpoint displacement–time histories of the SCS50 sandwich panel with simply supported and axially-restrained boundaries as well as the SCS75 sandwich panel with axially-restrained boundary are presented in Fig. 8.21. It can be seen that the maximum displacement of the axially-restrained SCS50 sandwich panel is reduced by 27% as compared to the simply supported panel. This can be attributed to the increase in resistance and ductility when the axially-restrained boundary is adopted. The FE simulations were also conducted to obtain the load (or resistance) versus displacement curve of the SCS sandwich panel under quasi-static uniform pressure loading. As demonstrated in Fig. 8.22, the maximum resistance and corresponding displacement of the axially-restrained SCS50 sandwich panel increase 268.0 and 93.9%, respectively, as compared to the simply supported panel. By comparing the SCS50 and SCS75 sandwich panels with axially-restrained boundary in Fig. 8.21, it is observed that the maximum displacement of the SCS75

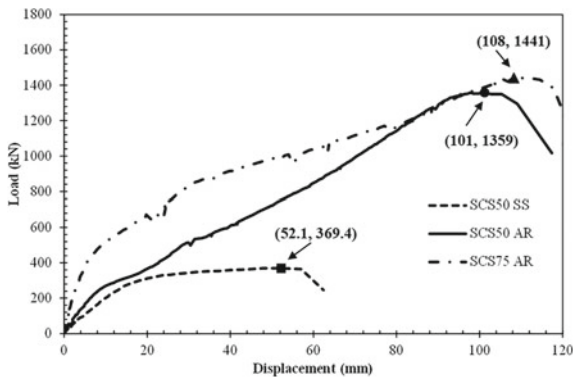


Fig. 8.22 Load–displacement curves of SCS sandwich panels under quasi-static uniform pressure loading

sandwich panel can be reduced by 37% through increasing the grout core depth owing to the enhanced load–displacement response (as shown in Fig. 8.22) and increased total mass.

Further analyzing the load–displacement curves of the SCS50 sandwich panel with simply supported and axially-restrained boundaries in Fig. 8.22 reveals that both of them are similar at initial stage. This indicates that the SCS50 sandwich panel mainly relies on the bending action to resist the load at initial stage. After the failure of grout core, the load was taken over by the tensile membrane of the steel plates that were axially restrained, while the simply supported panel behaved shear failure. By comparing the load–displacement curves of the axially-restrained SCS50 and SCS75 sandwich panels, the increase in grout core depth improved the resistance at initial stage, but shows little effect on the final resistance and ductility. This is because the grout core has minimal contribution to the resistance after severe cracking of grout.

Figure 8.23 presents the scaled damage measure contours of the SCS50 sandwich panel with simply supported and axially-restrained boundaries. The scaled damage measure, which is a function of accumulated effective plastic strain parameter λ , is defined in MAT_72R3 to evaluate the damage level of concrete. When it ranges from

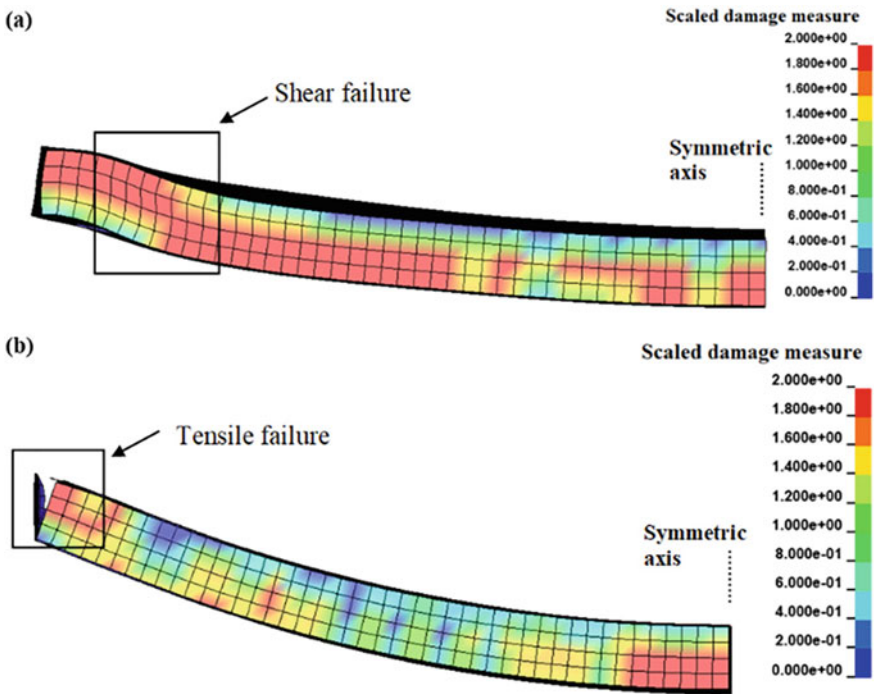


Fig. 8.23 Failure modes of SCS50 under quasi-static uniform pressure loading: **a** simply supported, **b** axially restrained

0 to 1, the material transitions from the yield failure surface to the maximum failure surface. When it ranges from 1 to 2, the material transitions from the maximum failure surface to the residual failure surface. The grout core of both the two panels underwent severe damage after failure. Shear failure mode can be seen from the plot for the simply supported SCS50 sandwich panel, while the tensile membrane failure is shown in the plot for the axially-restrained panel. Owing to the different failure modes, the resistance of the simply supported SCS sandwich panel is mainly governed by the shear strength of grout, while the failure strain of mild steel governs the resistance of the axially-restrained SCS sandwich panel.

8.4 Summary

The performances of SCS sandwich panels under impulsive loading were experimentally studied in this chapter. The impulsive loading was achieved in the laboratory by utilizing an inflated high pressure airbag to transfer the applied load from dropped projectile onto the panels. In addition, FE simulations on SCS sandwich panels under blast loading were also conducted. The main findings from the experimental and numerical studies are summarized as follows:

- (1) A combination of flexure and shear deformation mode was observed for the SCS sandwich panel under impulsive loading.
- (2) The maximum and permanent deformations of the SCS75 panel with thicker core were significantly smaller as compared to the SCS50 panel owing to the higher resistance and mass. The SCS75 panel also absorbed higher impact impulse under the same impact condition.
- (3) The debonding between the grout core and bottom plate during impact was observed from the strain–time histories of both the two tested SCS sandwich panels.
- (4) The established FE models of SCS sandwich panels were shown to be reasonable by comparing with the test results. The majority of energy was absorbed by steel plates owing to the higher strength and ductility as compared to the grout core.
- (5) The blast resistance of axially-restrained SCS sandwich panel could be significantly improved as compared to the simply supported counterpart owing to the enhanced resistance and ductility via developing tensile membrane of steel plates.

References

- Abramowicz W, Jones N (1986) Dynamic progressive buckling of circular and square tubes. *Int J Impact Eng* 4:243–270
- Anandavalli N, Lakshmanan N, Rajasankar J et al (2012) Numerical studies on blast loaded steel–concrete composite panels. *JCES* 1(3):102–108
- Arora H, Hooper PA, Dear JP (2011) Dynamic response of full–scale sandwich composite structures subject to air–blast loading. *Compos: Part A* 42:1651–1662
- ASCE (2010) Design of blast–resistant buildings in petrochemical facilities. American Society of Civil Engineers, Reston, Virginia
- ASCE (2011) Blast protection of buildings. American Society of Civil Engineers, Reston, Virginia
- Baker WE (1973) Explosions in air. University of Texas Press, Austin
- Chen W, Hao H (2014) Experimental investigations and numerical simulations of multi–arch double–layered panels under uniform impulsive loadings. *Int J Impact Eng* 63:140–157
- Chen W, Hao H, Chen S (2015) Numerical analysis of prestressed reinforced concrete beam subjected to blast loading. *Mater Des* 65:662–674
- Clubley SK (2014) Non–linear long duration blast loading of cylindrical shell structures. *Eng Struct* 59:113–126
- Crawford JE, Lan S (2006) Blast barrier design and testing. In: Proceedings of the ASCE Structures Congress, St. Louis, Missouri
- Crawford JE, Wu Y, Magallanes JM et al (2012) Modeling of concrete materials under extreme loads. *Advances in Protective Structures Research*, Taylor & Francis Group, London
- Foglar M, Kovar M (2013) Conclusions from experimental testing of blast resistance of FRC and RC bridge decks. *Int J Impact Eng* 59:18–28
- Grote DL, Park SW, Zhou M (2001) Dynamic behavior of concrete at high strain rate and pressure: I. experimental characterization. *Int J Impact Eng* 25:869–886
- Hallquist JO (2006) LS-DYNA theory manual. Livermore Software Technology Corporation (LSTC). Livermore, California
- Hallquist JO (2012) LS-DYNA keyword user’s manual. Livermore, California: Livermore Software Technology Corporation. Livermore, California
- Hou S, Zhao S, Ren L et al (2013) Crashworthiness optimization of corrugated sandwich panels. *Mater Des* 51:1071–1084
- Hyde D (1991) Conventional Weapons program (ConWep). US Army Waterways Experimental Station, Vicksbure
- Ishiguro S (2007) Experiments and analyses of fracture properties of grouting mortars. In: Proceedings of the 6th international conference on fracture mechanics of concrete and concrete structures
- Jiang H, Wang X, He S (2012) Numerical simulation of impact tests on reinforced concrete beams. *Mater Des*; 39:11–120
- Jing L, Xi C, Wang Z et al (2013) Energy absorption and failure mechanism of metallic cylindrical sandwich shells under impact loading. *Mater Des* 52: 470–480
- Jones N (1988) Structural impact. Cambridge University Press, New York
- Kilicaslan C, Guden M, Odaci IK et al (2012), The impact responses and the finite element modeling of layered trapezoidal corrugated aluminum core and aluminum sheet interlayer sandwich structures. *Mater Des* 46:121–133
- Lacroix DN, Doudak G, El–Domiatiy K (2014) Retrofit options for light–frame wood stud walls subjected to blast loading. *J Struct Eng* 140(4):04013104
- Lan S, Lok TS, Heng L (2005) Composite structural panels subjected to explosive loading. *Constr Build Mater* 19:387–395
- Liew JYR, Sohel KMA (2009) Lightweight steel–concrete–steel sandwich system with J–hook connectors. *Eng Struct* 31(5):1166–1178
- Liew JYR, Wang TY (2011) Novel steel–concrete–steel sandwich composite plates subjected to impact and blast load. *Adv Struct En* 14(4):673–686

- Liew JYR, Sohel KMA, Koh CG (2009) Impact tests on steel–concrete–steel sandwich beams with lightweight concrete core. *Eng Struct* 31(9):2045–2059
- Lin X, Zhang YX, Hazell PJ (2014) Modelling the response of reinforced concrete panels under blast loading. *Mater Des* 56:620–628
- Magallanes JM, Wu Y, Malvar LJ et al (2010) Recent improvements to release III of the K&C concrete model. In: the 11th international LS–DYNA users conference
- Malvar LJ, Crawford JE, Wesevich JW et al (1997) A plasticity concrete material model for DYNA3D. *Int J Impact Eng* 19:847–873
- Mao L, Barnett S, Begg D et al (2014) Numerical simulation of ultra high performance of fibre reinforced concrete panel subjected to blast loading. *Int J Impact Eng*; 64:91–100
- Mostaghel N (2003) Blast load simulation system. US Patent US06536258B1, 25 Mar 2003
- Remennikov AM, Liew JYR, Kong SY et al (2009) Simulation of impulsive loading on columns using an inflatable airbag technique. In: Proceedings of the 8th International Conference on Shock & Impact Loads on Structures, Adelaide, Australia
- Remennikov AM, Kong SY (2012) Numerical simulation and validation of impact response of axially-restrained steel–concrete–steel sandwich panels. *Compo Struct* 94:3546–3555
- Ross CA, Thompson PY, Tedesco JW (1989) Split–Hopkinson pressure–bar tests on concrete and mortar in tension and compression. *ACI Mater J* 86(5):475–481
- Schleyer GK, Lowak MJ, Polcyn MA et al (2007) Experimental investigation of blast wall panels under shock pressure loading. *Int J Impact Eng* 34:1095–1118
- Smith SJ, McCann DM, Kamara ME (2009) Blast resistant design guide for reinforced concrete structures. Portland Cement Association, Skokie
- Smith PD, Hetherington JG (1994) Blast and ballistic loading of structures. Butterworth–Heinemann, Oxford
- Sohel KMA, Liew JYR (2011) Steel–concrete–steel sandwich slabs with lightweight core–static performance. *Eng Struct* 33(3):981–992
- Symonds PS (1967) Survey of methods of analysis for plastic deformation of structures under dynamic loading. Division of Engineering Report BU/NSRDC/1–67, Brown University
- Tabatabaei ZS, Volz JS, Baird J et al (2013) Experimental and numerical analyses of long carbon fiber reinforced concrete panels exposed to blast loading. *Int J Impact Eng* 57:70–80
- UFC 3–340–02 (2008) Structures to resist the effects of accidental explosions. US Department of Army, Navy and the Air Force, Washington, DC
- Wang Y, Liew JYR, Lee SC (2015a) Experimental and numerical studies of non-composite Steel–Concrete–Steel sandwich panels under impulsive loading. *Mater Des* 81:104–112
- Wang Y, Liew JYR, Lee SC (2015b) Theoretical models for axially restrained steel–concrete–steel sandwich panels under blast loading. *Int J Impact Eng* 6:221–231
- Wu J, Chew SH (2014). Field performance and numerical modeling of multi–layer pavement system subject to blast load. *Constr Build Mater* 52:177–188
- Zhai X, Wang Y (2013) Modelling and dynamic response of steel reticulated shell under blast loading. *Shock Vib* 20(1):19–28
- Zhai X, Wang Y, Huang M (2013) Performance and protection approach of single–layer reticulated dome subjected to blast loading. *Thin-Walled Struct* 73:57–67